An IPT Battery Charger With Near Unity Power Factor and Load-Independent Constant Output Combating Design Constraints of Input Voltage and Transformer Parameters

Xiaohui Qu, *Member, IEEE*, Haijun Chu, Siu-Chung Wong, *Senior Member, IEEE*, and Chi K. Tse, *Fellow, IEEE*

***Abstract*—Inductive power transfer (IPT) techniques are becoming popular in battery charging applications due to some unique advantages compared to the conventional plug-in systems. A high-performance IPT charger should provide the battery with an efficient charging profile consisting of constant charging current and constant charging voltage. However, with a wide load range, it is hard to realize the initial load-independent constant current (CC) and the subsequent load-independent constant voltage (CV) using a single IPT converter while maintaining nearly unity power factor and soft switching of power switches simultaneously. This paper systematically analyzed the characteristics of an *LCC–LCC* compensated IPT converter and proposed a design method to realize the required load-independent CC and CV outputs at two zero-phase angle frequencies. The design also combats the constraints of an IPT transformer and input voltage, thus facilitating the use of a simple duty cycle control operating at two fixed frequencies for both CC and CV operations. The design criteria, control logic, and sensitivities of compensation parameters to the input impedance and load-independent output are discussed. Finally, an IPT battery charger prototype with 1 A charging current and 24 V battery voltage is built to verify the analysis.**

***Index Terms*—Inductive power transfer (IPT) battery charger, *LCC–LCC* compensation, load-independent outputs, soft switching, unity power factor.**

I. Introduction

THE use of inductive power transfer (IPT) techniques has gained popularity in battery charging applications, from the low-power battery charging of cell phones [1]–[3] to high-power battery charging of electric vehicles (EVs) [4]–[7]. Currently, the high-performance lithium-ion battery is being widely used in various energy storage applications with the advantages of high energy density, negligible memory effect, and low self-discharge rate. Fig. 1 shows a typical lithium-ion battery charging profile, where two dominant charging modes occur with an initial constant current (CC) mode and a subsequent constant voltage (CV) mode. The battery charging starts with CC mode while the battery voltage increases. When the battery voltage reaches a specified level, the charging process will change from CC to CV. The charging ends until the current decreases to near zero. Both the charging current for CC mode and the charging voltage for CV mode are specified by the material properties and inner connection of battery cells. To extend the battery lifetime and recycle time, an IPT charger should deliver current efficiently to the battery according to the charging profile.

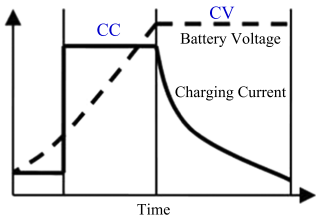

Fig. 1. Typical charging profile of a lithium-ion battery.

The transmitter and receiver in an IPT battery charger are the primary and secondary windings of a loosely coupled transformer, which has a relatively large amount of uncoupled magnetic flux fleeing into the air. It is well known that the output power can be dramatically maximized by operating the resonant transmitter and receiver at the same resonant frequency. Thus, the compensation circuits, which facilitate the formation of resonance tanks, are crucial in an IPT converter. As a resonant converter, the IPT converter has complex characteristics of output voltage, output current, input impedance, efficiency, etc., all of which involve transformer coupling and load variation. In the cell phone battery charging application, a charging platform with the uniform magnetic field is usually designed to avoid coupling variation [8], [9]. In the EV battery charging application, new technologies in smart EVs with self-driving and parking capabilities [10], [11] can minimize variations of

Manuscript received June 22, 2018; revised August 24, 2018 and October 22, 2018; accepted November 9, 2018. Date of publication November 13, 2018; date of current version May 22, 2019. This work was supported in part by the Natural Science Foundation of Jiangsu Province, China (BK20181280), in part by the Fundamental Research Funds for Central Universities of China, and in part by the Hong Kong RGC General Research Fund (PolyU 152082/17E). Recommended for publication by Associate Editor J. Acero. *(Corresponding author: Xiaohui Qu.)*

X. Qu and H. Chu are with the School of Electrical Engineering, Southeast University, Nanjing 210096, China (e-mail:

misalignment and coupling in both stationary and dynamic IPT charging applications. These technologies can be readily used in the existing IPT systems to improve the performance. However, the equivalent load of a battery in the charging process is always varying. From Fig. 1, the equivalent resistance as a ratio of the battery voltage to the charging current is increasing continuously and significantly from CC mode to CV mode of operations, which complicates the design of the IPT charger. To achieve the required output charging voltage and current, a variable frequency control is usually used to regulate the output voltage or current, whereas the input impedance may not be resistive, causing a large reactive power and increasing the component volt–ampere (VA) ratings. To eliminate the reactive power within the circuit, the variable frequency control may aim to realize a zero-phase angle (ZPA) between the input voltage and current, whilst the output voltage and current are regulated by a front-end converter or a downstream converter. Obviously, the additional power conversion stage makes the whole system uneconomical, bulky, and inefficient, although it has a wide range of regulation [7].

In view of the aforementioned issues, a well-designed compensation circuit of an IPT charger is expected to have a near resistive input impedance for decreasing component power ratings and load-independent CC and CV outputs for providing the inherent regulation against load variation. Moreover, a slight twist of frequency or modulation can achieve a slightly inductive input impedance for zero-voltage switching (ZVS) of MOSFETs and a slightly capacitive input impedance for zero-current switching of IGBTs that the converter efficiency can be further improved. At the input ZPA frequency, the series–series (SS) and parallel–parallel compensation networks can realize load-independent CC output, whereas the series-parallel and parallel-series compensation can realize load-independent CV output [12], [13]. However, the converter transfer function and the load-independent CC and CV properties of IPT converters using any of the four basic compensation networks are greatly restricted by the transformer parameters. Given a set of input voltage and transformer parameters, higher order compensation networks are introduced with greater design freedom for achieving the required CC and CV outputs [14]–[17]. To achieve the battery required initial CC and the subsequent CV charging, an IPT converter can operate at two separate frequencies. However, only one operating frequency can achieve input ZPA, and the other operating frequency will be reactive. Such a design has been implemented in [18] by using the SS compensation and in [19] by using the *LCC–LCC* compensation to realize the load-independent CC output at ZPA frequency and load-independent CV output at non-ZPA frequency that may come with significant reactive power and large component stresses. Some hybrid topologies are proposed by integrating two sets of compensation circuits operating at a single ZPA frequency, where one set of compensation circuits realizes the load-independent CC output and the other set of compensation circuits realizes the load-independent CV output [20], [21]. The mode transition depends on some bidirectional power switches, usually implemented by two MOSFETs or IGBTs in anti-series or anti-parallel configuration. These bidirectional power switches are dissipative components on the power path that their losses can be significant.

It is desirable that an IPT converter has at least two load-independent ZPA operating frequencies, one with a CC output and the other with a CV output, satisfying the charging profile of the battery. Vu *et al.* [22] have proved that the *LCC–LCC* compensated IPT converter has ZPA operating frequencies for both CC and CV outputs. However, transformer parameters in [22] must be designed for the required set of design constraints, which include two ZPA operating frequencies, and load-independent CC and CV outputs. In many applications, the IPT transformer is often space constrained, and the transformer parameters should be included the set of design constraints instead of the set of design parameters in [22], which also makes it impossible to perform optimization in CC and CV output amplitudes. Without an additional front-end converter or a downstream converter, the output charging current and voltage cannot be regulated for the required battery charging profile. To address these issues, this paper gives a systematical analysis of the *LCC–LCC* compensated IPT charger. From the characteristics analyzed, a design method for the IPT charger is proposed. Given a set of design constraints that includes the required load-independent CC and CV outputs for charging the battery, an IPT transformer, and an input dc voltage with a small variation, compensation components in the *LCC–LCC* network are designed by using a simple duty cycle control operating at two fixed frequencies to realize the initial CC charging and the subsequent CV charging of the battery. The sensitivities of input impedance, output current and voltage to the variations of compensation parameters, and their effects on achieving soft switching for the required outputs are also discussed in detail. Finally, a prototype of the IPT charger with 1 A charging current and 24 V battery voltage is built to verify the analysis in this paper.

Specifically, Section II analyzes the construction method of the *LCC–LCC* compensation network with at least two ZPA frequencies for both load-independent CC output and load-independent CV output. The design to combat the constraints due to the IPT transformer and input voltage are derived theoretically for battery chargers. Section III shows the detailed implementation of the system with frequency selection, control logic, sensitivity analysis, and ZVS realization. The performance of the *LCC–LCC* compensated IPT charger is evaluated in Section IV. Finally, Section V concludes this paper.

II. Construction of *LCC–LCC* Compensation Network With Two ZPA Frequencies for Load-Independent CC and CV Outputs

As discussed in Section I, for battery charging applications, an *LCC–LCC* compensated IPT converter should be designed with input ZPA at two operating angular frequencies $\omega_{\rm CC}$ and $\omega_{\rm CV}$ for load-independent CC and load-independent CV outputs, given any input dc voltage and transformer parameters.

To facilitate the analysis, the IPT converter using *LCC–LCC* compensation is driven by a pure sinusoidal ac voltage source $v_{\rm IN}$ with an angular frequency ω, and delivers power to an

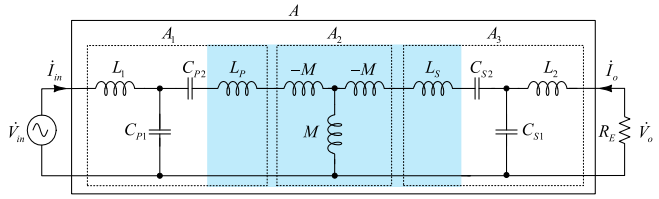

Fig. 2. Schematic of an *LCC–LCC* compensated IPT converter as a two-port network, where the T model of loosely coupled transformer is in shaded area.

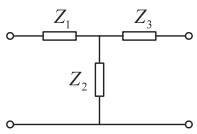

Fig. 3. Typical T network.

equivalent load R_E, as shown in Fig. 2. The loosely coupled transformer is modeled as a three-parameter T network where L_P and L_S are the self-inductances of the primary side and secondary side, and M is the mutual inductance. L_P and L_S are independent. The primary *LCC* network is composed by the external elements L_1, C_{P1}, and C_{P2}, whereas the secondary *LCC* network is composed by L_2, C_{S1}, and C_{S2}. $\dot{V}_{\rm in}$, $\dot{I}_{\rm in}$, $\dot{V}_o$, and $\dot{I}_o$ are phasor variables of $v_{\rm IN}$, $i_{\rm IN}$, v_O, and i_O, respectively.

A. Acquisition of $\omega_{\rm CC}$ With Load-Independent CC Output

The IPT converter can be simplified as a two-port network with the transmission matrix A, as shown in Fig. 2, where A satisfies

$$\left[\dot{V}_{\rm in}, \dot{I}_{\rm in}\right]^T = A\left[\dot{V}_o, -\dot{I}_o\right]^T. \tag{1}$$

The network can be further decomposed into three cascading subnetworks with the transfer matrices satisfying

$$A = A_1 A_2 A_3. \tag{2}$$

Each subnetwork is a typical T network. It is known that the input impedance of a T network is purely resistive under the condition of $Z_1 = -Z_2 = Z_3$, as shown in Fig. 3. Besides, by applying Thévenin's and Norton's theorems, if L_1 and C_{P1} in the subnetwork of A_1 are in resonance at ω, subnetwork A_1 fed by the input voltage source $\dot{V}_{\rm in}$ can be converted to a load-independent current source, as shown in Fig. 4. Because M and $-M$ in subnetwork A_2 must be in resonance at some frequency, subnetwork A_2 fed by a current source can be transformed to a load-independent voltage source. If L_2 and C_{S1} in subnetwork A_3 are in resonance at ω, subnetwork A_3 fed by a voltage source can be transformed to a load-independent current source $\frac{M\dot{V}_{\rm in}}{j\omega_{\rm CC}L_1L_2}$, which can charge the battery load directly. Considering the ZPA realization condition of $Z_1 = -Z_2 = Z_3$ for a T network, the *LCC–LCC* compensation parameters should satisfy (3), where the resonant angular frequency ω is rewritten as $\omega_{\rm CC}$, i.e.,

$$\begin{cases} \omega_{\rm CC}L_1 = \frac{1}{\omega_{\rm CC}C_{P1}} = \omega_{\rm CC}L_P - \frac{1}{\omega_{\rm CC}C_{P2}} \text{ and} \\ \omega_{\rm CC}L_2 = \frac{1}{\omega_{\rm CC}C_{S1}} = \omega_{\rm CC}L_S - \frac{1}{\omega_{\rm CC}C_{S2}}. \end{cases} \tag{3}$$

Thus, the angular frequency ω of $v_{\rm IN}$ should be tuned at $\omega_{\rm CC}$ for the CC mode charging. The charging current $\dot{I}_o$ is given by

$$\dot{I}_o = -\frac{M\dot{V}_{\rm in}}{j\omega_{\rm CC}L_1L_2}. \tag{4}$$

Obviously, more design freedom of the output CC can be achieved by adjusting the external inductors L_1 and L_2.

B. Acquisition of $\omega_{\rm CV}$ With Load-Independent CV Output

To find another operating frequency that achieves the load-independent voltage output, it is assumed that the operating angular frequency $\omega = \alpha\omega_{\rm CC}$. The external inductors L_1 and L_2 are further defined as

$$L_1 = \xi_1 L_P \text{ , and } L_2 = \xi_2 L_S. \tag{5}$$

Using (3), the external capacitors C_{P1}, C_{P2}, C_{S1}, and C_{S2} can be expressed as $\frac{\alpha^2}{\omega^2 L_P \xi_1}$, $\frac{\alpha^2}{\omega^2 L_P (1-\xi_1)}$, $\frac{\alpha^2}{\omega^2 L_S \xi_2}$, and $\frac{\alpha^2}{\omega^2 L_S (1-\xi_2)}$ at $\alpha\omega_{\rm CC}$. Here, ξ_1 and ξ_2 are restricted by inequalities given by $0 < \xi_1 < 1$ and $0 < \xi_2 < 1$ to ensure that C_{P2} and C_{S2} are non-zero capacitors. If $\xi_1 = 1$ and $\xi_2 = 1$, impedances of C_{P2} and C_{S2} are zero, which is actually the *LC–LC* compensation [24], [25]. The equivalent parameters operating at $\alpha\omega_{\rm CC}$ are shown in Fig. 5. Thus, matrices A_1, A_2, and A_3 are given by

$$\begin{cases} A_1 = \begin{bmatrix} 1-\alpha^2 & j\omega L_P\left(2-\alpha^2-\frac{1-\xi_1}{\alpha^2}\right) \\ \frac{j\alpha^2}{\xi_1\omega L_P} & \frac{(1-\alpha^2)}{\xi_1} \end{bmatrix} \\ A_2 = \begin{bmatrix} 0 & -j\omega M \\ \frac{1}{j\omega M} & 0 \end{bmatrix} \\ A_3 = \begin{bmatrix} \frac{(1-\alpha^2)}{\xi_2} & j\omega L_S\left(2-\alpha^2-\frac{1-\xi_2}{\alpha^2}\right) \\ \frac{j\alpha^2}{\xi_2\omega L_S} & 1-\alpha^2 \end{bmatrix}. \end{cases} \tag{6}$$

It is found that all elements in the diagonal of A_1, A_2, and A_3 are real and all off-diagonal elements are imaginary. Thus, A in (2) can be expressed as

$$A = \begin{bmatrix} a_{11} & ja_{12} \\ ja_{21} & a_{22} \end{bmatrix} \tag{7}$$

where a_{11}, a_{12}, a_{21}, and a_{22} are all real. Substituting (6) into (2), we have

$$\begin{cases} a_{11} = \left[\frac{L_P}{\xi_2 M}\left(2-\alpha^2-\frac{1-\xi_1}{\alpha^2}\right)+\frac{M}{\xi_2 L_S}\alpha^2\right](1-\alpha^2) \\ a_{12} = \omega\frac{L_P L_S}{M}\left(2-\alpha^2-\frac{1-\xi_1}{\alpha^2}\right)\left(2-\alpha^2-\frac{1-\xi_2}{\alpha^2}\right) \\ \qquad -\omega M(1-\alpha^2)^2 \\ a_{21} = -\frac{(1-\alpha^2)^2}{\omega\xi_1\xi_2 M}+\frac{\alpha^4 M}{\omega\xi_1\xi_2 L_P L_S} \\ a_{22} = \left[\frac{L_S}{\xi_1 M}\left(2-\alpha^2-\frac{1-\xi_2}{\alpha^2}\right)+\frac{M}{\xi_1 L_P}\alpha^2\right](1-\alpha^2). \end{cases} \tag{8}$$

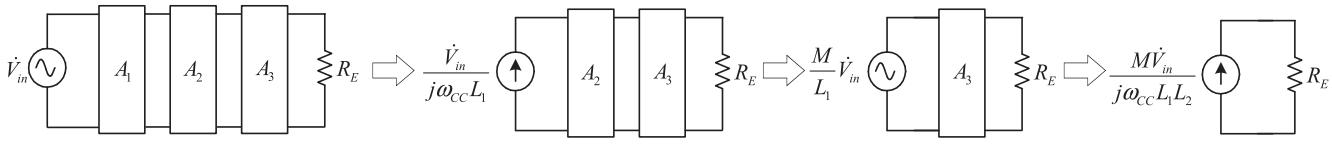

Fig. 4. Derivation of the load-independent CC output for an *LCC–LCC* compensated IPT converter.

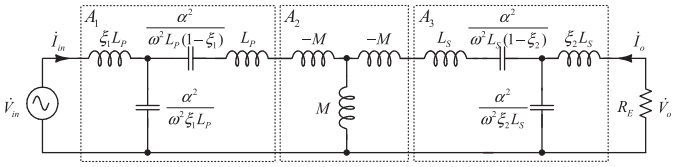

Fig. 5. Schematic of the IPT converter in Fig. 2 operating at another angular frequency $\alpha\omega_{CC}$.

To have ω qualified as an input ZPA frequency, the input impedance is obtained as

$$Z_{\mathrm{IN}} = \frac{\dot{V}_{\mathrm{in}}}{\dot{I}_{\mathrm{in}}} = \frac{a_{11}R_E + ja_{12}}{a_{22} + ja_{21}R_E} \tag{9}$$

$$= \frac{(a_{11}a_{22} + a_{21}a_{12})R_E + j(a_{12}a_{22} - a_{11}a_{21}R_E^2)}{{a_{22}}^2 + {a_{21}}^2 R_E^2}. \tag{10}$$

Z_{IN} is expected to be purely resistive, which implies $a_{12}a_{22} - a_{11}a_{21}R_E^2 = 0$ for any R_E. Hence, we have

$$a_{12}a_{22} = 0 \text{ and } a_{11}a_{21} = 0. \tag{11}$$

As the two-port network A only consists of linear passive inductors, capacitors, and parasitic resistors, it is a reciprocal network. By the principle of reciprocity, the elements of A satisfy

$$a_{11}a_{22} + a_{12}a_{21} = 1. \tag{12}$$

Solving (11) and (12), two possible solutions are given as follows:

$$\begin{cases} \text{Case 1: } a_{11} = 0 \text{ and } a_{22} = 0. \\ \text{Case 2: } a_{12} = 0 \text{ and } a_{21} = 0. \end{cases} \tag{13}$$

For Case 1, $a_{11} = 0$ and $a_{22} = 0$, we have $a_{12}a_{21} = 1$. The matrix is rewritten as

$$\begin{bmatrix} \dot{V}_{\mathrm{in}} \\ \dot{I}_{\mathrm{in}} \end{bmatrix} = A \begin{bmatrix} \dot{V}_o \\ -\dot{I}_o \end{bmatrix} = \begin{bmatrix} 0 & ja_{12} \\ ja_{21} & 0 \end{bmatrix} \begin{bmatrix} \dot{V}_o \\ -\dot{I}_o \end{bmatrix}. \tag{14}$$

The corresponding solution is given by

$$\dot{I}_o = -\frac{\dot{V}_{\mathrm{in}}}{ja_{12}} = ja_{21}\dot{V}_{\mathrm{in}}. \tag{15}$$

Obviously, in Case 1, there is no ZPA frequency for the load-independent CV output. Substituting $a_{11} = 0$ and $a_{22} = 0$ into (8) and solving, the only solution is $\alpha = 1$, i.e., $\omega = \omega_{CC}$. In addition, if $\xi_1 = \xi_2 = \xi$, load-independent CC output can be achieved at two frequencies $\alpha_1\omega_{CC}$ and $\alpha_2\omega_{CC}$, where $\alpha_{1,2} = \sqrt{\frac{1 \pm \sqrt{1-(1-k^2)(1-\xi)}}{1-k^2}}$. Here, k is the coupling coefficient of the loosely coupled transformer given by $k = \frac{M}{\sqrt{L_P L_S}}$. Fig. 6 shows an example with $f_{\mathrm{CC}} = \frac{\omega_{\mathrm{CC}}}{2\pi} = 200$ kHz and $k = 0.367$. If ξ_1 and ξ_2 are designed equal to 0.1, there are another two frequencies $f_{\mathrm{CC1}} = \alpha_1 f_{\mathrm{CC}} = 156$ kHz and $f_{\mathrm{CC2}} = \alpha_2 f_{\mathrm{CC}} = 260$ kHz to satisfy the load-independent CC output and input ZPA simultaneously.

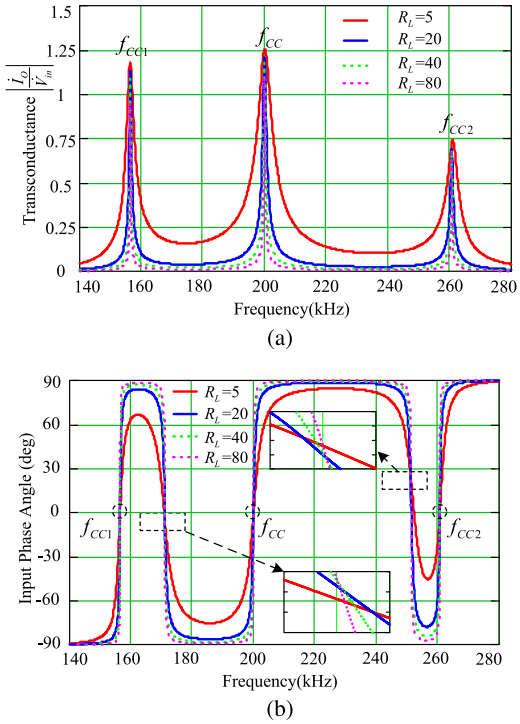

Fig. 6. Three frequencies f_{CC}, f_{CC1}, and f_{CC2} for (a) load-independent CC output, and (b) input ZPA as an example of $k = 0.367$ and $\xi_1 = \xi_2 = 0.1$.

For Case 2, $a_{12} = 0$ and $a_{21} = 0$, we have $a_{11}a_{22} = 1$. The matrix is rewritten as

$$\begin{bmatrix} \dot{V}_{\mathrm{in}} \\ \dot{I}_{\mathrm{in}} \end{bmatrix} = A \begin{bmatrix} \dot{V}_o \\ -\dot{I}_o \end{bmatrix} = \begin{bmatrix} a_{11} & 0 \\ 0 & a_{22} \end{bmatrix} \begin{bmatrix} \dot{V}_o \\ -\dot{I}_o \end{bmatrix}. \tag{16}$$

The corresponding solution is given by

$$\dot{V}_o = \frac{\dot{V}_{\mathrm{in}}}{a_{11}} = a_{22}\dot{V}_{\mathrm{in}}. \tag{17}$$

Substituting $a_{12} = 0$ and $a_{21} = 0$ into (8) and solving, solutions exist under two conditions of $\frac{1}{\xi_1} + \frac{1}{\xi_2} = \frac{(1\pm k)^2}{k^2}$.

1) If $\frac{1}{\xi_1} + \frac{1}{\xi_2} = \frac{(1-k)^2}{k^2}$

$$\dot{V}_o = -\sqrt{\frac{L_S}{L_P}\frac{\xi_2}{\xi_1}}\dot{V}_{\mathrm{in}} \text{ and } \alpha_{\mathrm{CV}} = \sqrt{\frac{1}{1-k}} > 1. \tag{18}$$

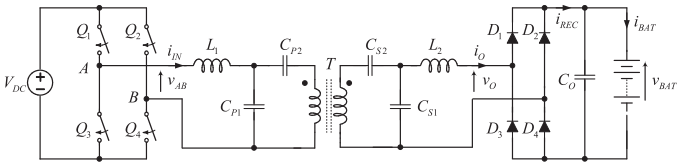

Fig. 7. *LCC–LCC* compensated IPT charger.

2) If $\frac{1}{\xi_1}+\frac{1}{\xi_2}=\frac{(1+k)^2}{k^2}$

$$\dot{V}_o=\sqrt{\frac{L_S}{L_P}}\frac{\xi_2}{\xi_1}\dot{V}_{\rm in} \text{ and } \alpha_{\rm CV}=\sqrt{\frac{1}{1+k}}<1. \quad (19)$$

C. Design Criteria for Battery Charging

From the above-mentioned analysis, the selection of ξ_1 and ξ_2, i.e., L_1 and L_2 plays an important role in the compensation characteristics. For a given input voltage, output charging profile, and IPT transformer, $\xi_1, \xi_2, \omega_{\rm CC}$, and $\omega_{\rm CV}$ can be uniquely determined by solving the following equations:

$$\begin{cases} \dot{I}_o=-\frac{M\dot{V}_{\rm in}}{j\omega_{\rm CC}L_PL_S\xi_1\xi_2}\frac{1}{\xi_1}+\frac{1}{\xi_2}=\frac{(1\pm k)^2}{k^2} \\ \dot{V}_o=\pm\sqrt{\frac{L_S}{L_P}}\frac{\xi_2}{\xi_1}\dot{V}_{\rm in} \\ \omega_{\rm CV}=\omega_{\rm CC}\sqrt{\frac{1}{1\pm k}}. \end{cases} \quad (20)$$

With the calculated values of ξ_1 and ξ_2, L_1 and L_2 can be found by (5). Then, the other compensation components of C_{P1}, C_{P2}, C_{S1}, and C_{S2} can be obtained by solving (3). In this way, an *LCC–LCC* compensated IPT charger can realize the input ZPA and output initial CC and subsequent CV operations, satisfying the constraints imposed by the input voltage and transformer parameters. Here, two groups of $\omega_{\rm CC}$, $\omega_{\rm CV}$ and their corresponding compensation parameters are available, whose selection depends on the application and its specified frequencies. If the frequencies are confirmed, a simple fixed frequency control operating at two frequencies $\omega_{\rm CC}$ and $\omega_{\rm CV}$ for both charging modes can fulfill all design requirements.

III. Design and Implementation of an *LCC–LCC* Compensated IPT Charger

As analyzed in Section II, an IPT charger using *LCC–LCC* compensation, as shown in Fig. 7, can be designed. The full-bridge switches $Q_{1,2,3,4}$ operate at $\omega_{\rm CC}$ or $\omega_{\rm CV}$ to generate a square voltage $v_{\rm AB}$. Here, the input dc voltage $V_{\rm DC}$ can be modulated by $Q_{1,2,3,4}$ with D being the duty cycle of $v_{\rm AB}$ half cycle. The fundamental component of $v_{\rm AB}$, denoted as $v_{\rm IN}$, is given as

$$v_{\rm IN}(t)=\frac{4V_{\rm DC}}{\pi}\sin\frac{\pi D}{2}\sin(\omega t+\theta). \quad (21)$$

A full-bridge diode rectifier and C filter are used to rectify the ac output current and filter the ripple voltage before connecting to the output battery. The specified voltage and current of the battery are $V_{\rm BAT}$ and $I_{\rm BAT}$, respectively. Fig. 8 shows the input and output waveforms of the secondary rectifier.

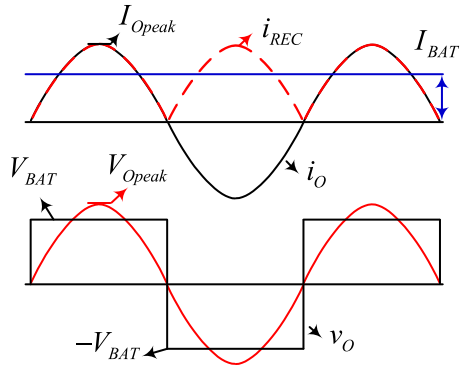

Fig. 8. Waveforms of the IPT secondary rectifier.

Using (4) and (21), the equivalent output current after the full-bridge rectification in CC mode is given by

$$I_{\rm BAT}=\frac{2I_{\rm O_{peak}}}{\pi}=\frac{8}{\pi^2}\frac{V_{\rm DC}\sin\frac{\pi D}{2}}{\omega_{\rm CC}L_PL_S\xi_1\xi_2}. \quad (22)$$

Using (18), (19), and (21), the output voltages in CV mode under both conditions are the same and given as

$$V_{\rm BAT}=\frac{\pi V_{\rm O_{peak}}}{4}=\sqrt{\frac{L_S}{L_P}}\frac{\xi_2}{\xi_1}V_{\rm DC}\sin\frac{\pi D}{2}. \quad (23)$$

Given an IPT transformer, input voltage, and the required battery voltage and current, the design of ξ_1, ξ_2, and $\omega_{\rm CC}$ is achieved by solving (22), (23), and $\frac{1}{\xi_1}+\frac{1}{\xi_2}=\frac{(1\pm k)^2}{k^2}$. The results are given by

$$\begin{cases} \xi_1=\frac{L_1}{L_P}=\frac{k^2}{(1\pm k)^2}\left(1+\frac{V_{\rm DC}\sin\frac{\pi D}{2}}{V_{\rm BAT}}\sqrt{\frac{L_S}{L_P}}\right) \\ \xi_2=\frac{L_2}{L_S}=\frac{k^2}{(1\pm k)^2}\left(1+\frac{V_{\rm BAT}}{V_{\rm DC}\sin\frac{\pi D}{2}}\sqrt{\frac{L_P}{L_S}}\right) \\ \omega_{\rm CC}=\frac{8}{\frac{\pi^2 I_{\rm BAT}k^3}{(1\pm k)^4}\left(\sqrt{\frac{L_S}{V_{\rm BAT}}}+\frac{\sqrt{L_PV_{\rm BAT}}}{V_{\rm DC}\sin\frac{\pi D}{2}}\right)^2}. \end{cases} \quad (24)$$

Substituting ξ_1, ξ_2, and $\omega_{\rm CC}$ into (3), the *LCC–LCC* parameters of L_1, C_{P1}, C_{P2}, L_2, C_{S1}, and C_{S2} can be calculated. To permit the ZVS turning-ON of MOSFETs $Q_{1,2,3,4}$, the input impedance should be slightly inductive in both modes of CC and CV. Fig. 9 shows the phase angles of input impedance versus the different normalized parameters and load conditions for the two modes of operation. During the charging process, the battery equivalent load $R_{\rm BAT}$ increases from $R_{\rm min}$ in CC mode, $R_{\rm mid}$ at the mode transition, to $R_{\rm max}$ in CV mode. From Fig. 9, in both CC and CV modes, a slight increment of L_1 and decrements of C_{P1} and C_{P2} will fulfill the objective. Additionally, the sensitivity of parameters to the converter output voltage and current should be inspected. The normalized output current in CC mode and the normalized output voltage in CV mode versus the normalized parameters of L_1, C_{P1}, and C_{P2} are shown in Fig. 10. Obviously, the variation of L_1 is not sensitive to both the output current and output voltage in the two modes of operation. Thus, a small increment of L_1 facilitates the ZVS realization of $Q_{1,2,3,4}$.

The operating frequency $\omega_{\rm CV}$ in CV mode can also be calculated by $\omega_{\rm CV}=\omega_{\rm CC}\sqrt{\frac{1}{1\pm k}}$. Thus, the duty cycle control under

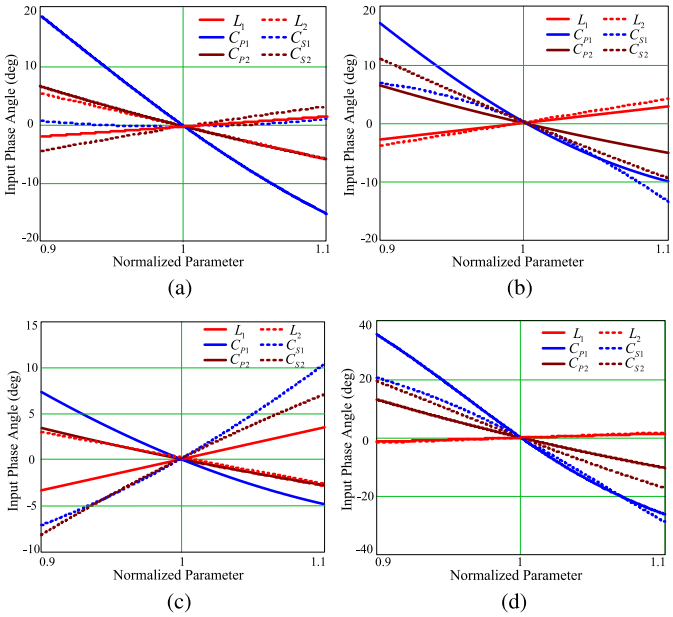

Fig. 9. Phase angle of input impedance versus normalized parameters. (a) CC mode: $R_{\mathrm{BAT}} = R_{\mathrm{min}}$. (b) CC mode: $R_{\mathrm{BAT}} = R_{\mathrm{mid}}$. (c) CV mode: $R_{\mathrm{BAT}} = R_{\mathrm{mid}}$. (d) CV mode: $R_{\mathrm{BAT}} = R_{\mathrm{max}}$.

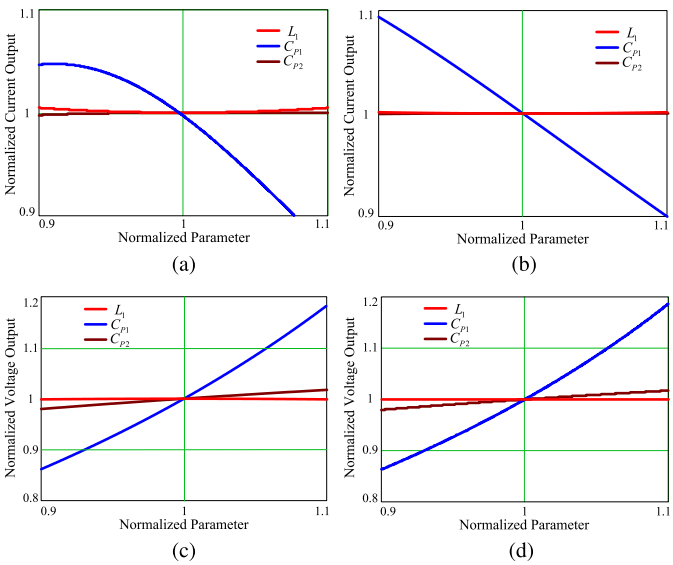

Fig. 10. Normalized output with varying normalized parameters. (a) CC mode: $R_{\mathrm{BAT}} = R_{\mathrm{min}}$. (b) CC mode: $R_{\mathrm{BAT}} = R_{\mathrm{mid}}$. (c) CV mode: $R_{\mathrm{BAT}} = R_{\mathrm{mid}}$. (d) CV mode: $R_{\mathrm{BAT}} = R_{\mathrm{max}}$.

two fixed switching frequencies f_{CC} and f_{CV} can be used to adjust the required output battery current and voltage. Fig. 11 shows the control logic, where the first CC operation enables the current loop to realize the required CC charging, i.e., $v_{\mathrm{enCC}} = 1$ and $v_{\mathrm{enCV}} = 0$. The duty cycle is generated by a sawtooth waveform with frequency f_{CC}. When the battery voltage rises to the specified level V_{ref}, the current loop is closed with $v_{\mathrm{enCC}} = 0$ and the voltage control loop with $v_{\mathrm{enCV}} = 1$ is activated with operating frequency f_{CV}. In this way, any small variation in input voltage, transformer parameters, and compensation parameters and output voltage or current drop due to the

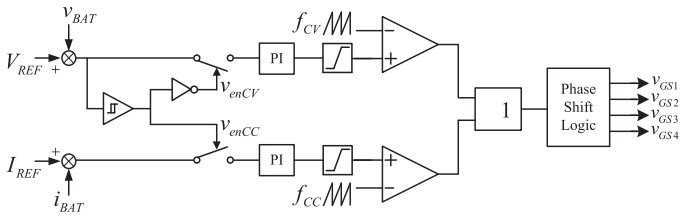

Fig. 11. Schematic of control logic for the IPT charger.

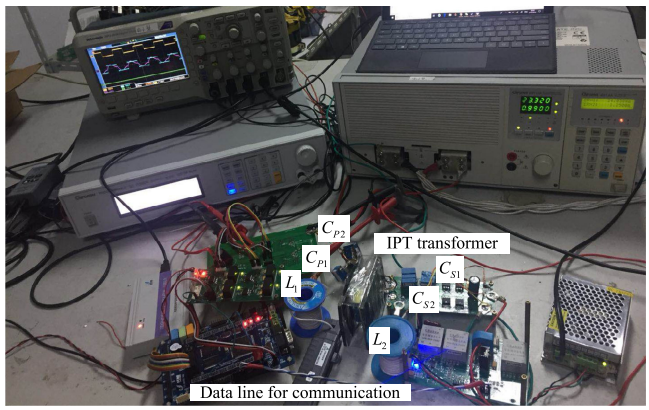

Fig. 12. Photo of the prototype IPT charger.

TABLE I
CALCULATED PARAMETERS FOR TWO CONDITIONS IN CV MODE

Condition	ξ_1	ξ_2	f_{CC}	f_{CV}
$\frac{1}{\xi_1} + \frac{1}{\xi_2} = \frac{(1-k)^2}{k^2}$	0.794	0.583	206.6 kHz	259.9 kHz
$\frac{1}{\xi_1} + \frac{1}{\xi_2} = \frac{(1+k)^2}{k^2}$	0.17	0.125	4.493 MHz	3.843 MHz

component parasitic resistance can be easily compensated by the feedback controller with the required charging current and voltage and ZVS operation.

IV. EXPERIMENTAL EVALUATION

To verify the above-mentioned analysis, a prototype IPT charger using *LCC–LCC* compensation has been built to charge a battery with 1 A charging current and 24 V battery voltage, as shown in Fig. 12. The input dc voltage is 32 V and the duty cycle D is designed as 0.95. An arbitrary IPT transformer is constructed, which is measured with parameters $L_P = 16.18\ \mu$H, $L_S = 15.52\ \mu$H, $M = 5.82\ \mu$H, and $k = 0.367$. The calculated ξ_1, ξ_2, f_{CC}, and f_{CV} for both conditions of CV mode operation are given in Table I. Here, $f_{\mathrm{CC}} = 206.6$ kHz and $f_{\mathrm{CV}} = 259.9$ kHz are chosen, where the design of inverter and magnetic components is relatively easy. In some applications, the frequency may be within a design specification, such as cell phone battery charging with Qi standard. If the two operating frequencies do not fall within a design specification, inductances L_P and/or L_S can be adjusted with smaller values for higher f_{CC} and f_{CV}, and vice versa, according to analytical equations (20) and (24). This may not be possible or can be very time consuming by using the numerical iteration given in [22]. Here, we

TABLE II
CALCULATED AND MEASURED PARAMETERS FOR *LCC–LCC* COMPENSATION NETWORK

Parameter	Calculated	Measured
L_1	12.84 μH	13.54 μH
C_{P1}	46.21 nF	45.73 nF
C_{P2}	177.9 nF	178.2 nF
L_2	9.048 μH	9.12 μH
C_{S1}	65.59 nF	64.9 nF
C_{S2}	91.73 nF	91.21 nF

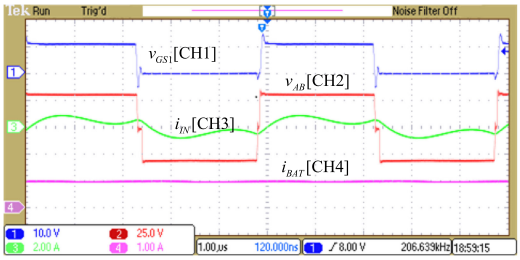

(a)

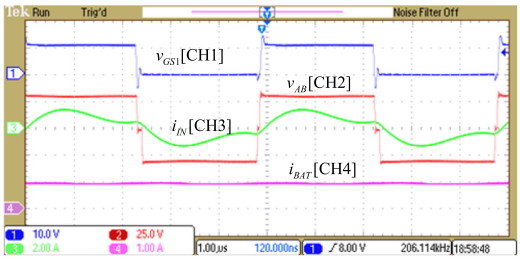

(b)

Fig. 13. Experimental waveforms of v_{GS1}, v_{AB}, i_{IN}, and i_{BAT} in CC charging mode and R_{BAT} of (a) 12 Ω and (b) 24 Ω.

accept the designed values of L_P and L_S and thus the operating frequencies f_{CC} and f_{CV}. The calculated and experimental parameters in the *LCC–LCC* compensation circuit are listed in Table II according to the equations given in Section III. To realize the ZVS, the experimental value of L_1 is chosen to be slightly larger than the calculated value. From the sensitivity analysis of these components, the experimental values of C_{P1}, C_{P2}, L_2, C_{S1}, and C_{S2} are consistent with the calculated results for the required battery charging current and voltage. The output filter uses C_O of 220 μF. Switches $Q_{1,2,3,4}$ are IRF530 and secondary rectifier diodes are MBRB3030CT. A dc electronic load from Chroma is used to emulate the EV battery. A phase-shift control is used here with a fixed frequency duty cycle control. A feedback control using the digital controller TMS320F28335 is applied to realize the two fixed frequencies transition. The sensed signals can be feed back wirelessly using the mature wireless communication technology in [7] and [26].

At the beginning of charging, the battery current should be kept at 1 A with the equivalent battery load $R_{\mathrm{BAT}} = \frac{v_{\mathrm{BAT}}}{i_{\mathrm{BAT}}}$ increasing, whereas the battery voltage is increasing toward the required 24 V. During the CC charging phase, v_{enCV} is 0 and v_{enCC} is 1, as shown in Fig. 11. The controller enables the current feedback loop at operating frequency f_{CC}. Fig. 13 shows the measured waveforms of gate drive voltage v_{GS1}, modulated voltage v_{AB}, input current i_{IN}, and output current i_{BAT} in CC

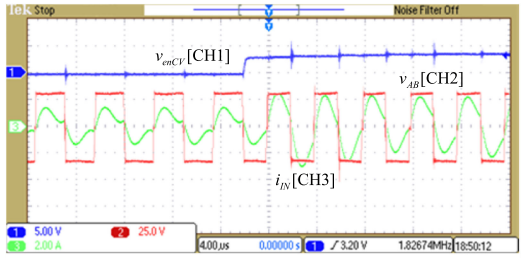

(a)

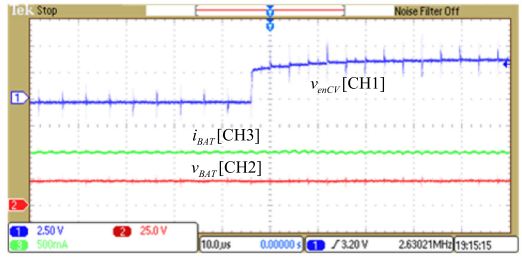

(b)

Fig. 14. Transient waveforms from CC mode to CV mode with mode enable signal v_{enCV} and (a) v_{AB}, i_{IN} and (b) i_{BAT} and v_{BAT}.

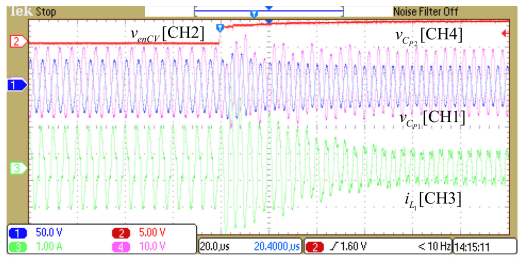

(a)

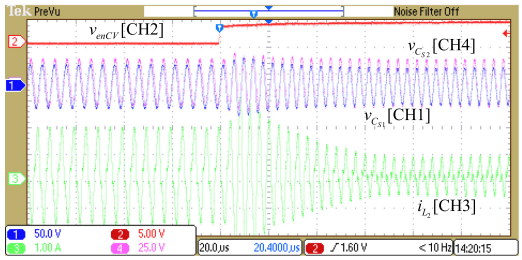

(b)

Fig. 15. Transient waveforms from CC mode to CV mode with mode enable signal v_{enCV} and (a) v_{CP1}, v_{CP2}, i_{L1} and (b) v_{CS1}, v_{CS2}, i_{L2}.

charging mode for two values of R_{BAT}, i.e., 12 Ω and 24 Ω. The battery current is kept at 1 A under CC charging. The waveform of i_{IN} is always nearly in phase with v_{AB}, which illustrates that the IPT charger has been well compensated with nearly zero reactive power, and the small phase angle of i_{IN} lagging v_{AB} ensures the ZVS of the full-bridge switches. When R_L reaches 24 Ω, i.e., v_{BAT} arrives at the required 24 V, and the charging process transits from CC mode to CV mode. Voltage v_{enCV} is 1 and v_{enCC} is 0. The controller in Fig. 11 disables the current loop and enables the voltage feedback loop at operating frequency f_{CV}. Fig. 14(a) shows the operating frequency changing from f_{CC} to f_{CV}, whereas the battery voltage v_{BAT}

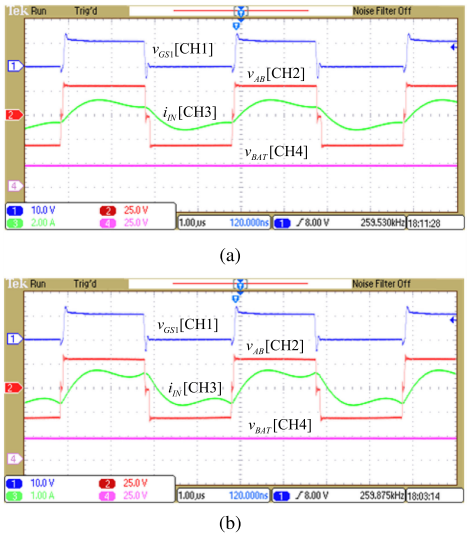

Fig. 16. Experimental waveforms of v_{GS1}, v_{AB}, i_{IN}, and v_{BAT} in CV charging mode and R_{BAT} of (a) 24 and (b) 48 Ω.

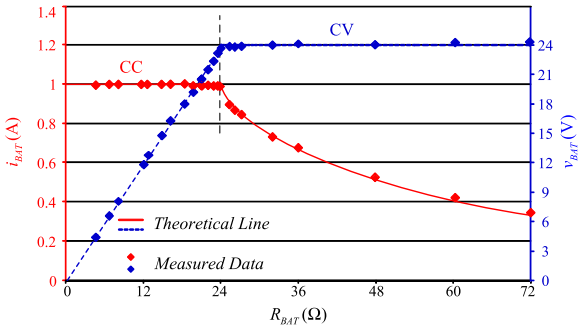

Fig. 17. Measured charging process versus the equivalent battery load.

and current i_{BAT} change smoothly during the mode transition, as shown in Fig. 14(b). The current across each compensation inductor and the voltage over each compensation capacitor before and after the mode transition are also given in Fig. 15. The steady-state waveforms of v_{GS1}, v_{AB}, i_{IN}, and v_{BAT} in CV charging mode are shown in Fig. 16(a) and (b) for R_{BAT} being 24 and 48 Ω. At the new operating frequency f_{CV}, the required load-independent CV output, near ZPA input and ZVS realization of $Q_{1,2,3,4}$ are all achieved, giving low power stresses and high transfer efficiency.

The whole charging process is shown in Fig. 17. The experimental data are consistent with the theoretical piecewise-linear curve. The measured efficiency using Yokogawa WT1800E power analyzer is shown in Fig. 18 for the whole charging process, where the efficiency sag at the mode transition is due to the smaller current flowing into primary and secondary windings of the transformer in CC mode as a result of the changing impedance at different operating frequencies. The power loss breakdown among the circuit components is shown in Fig. 19, when the power transfer efficiency is highest at R_{BAT} of 24 Ω in CC mode. The power losses in the compensation inductors, IPT transformer primary and secondary windings, MOSFETs, and rectifier diodes can be calculated by their inner resistances and

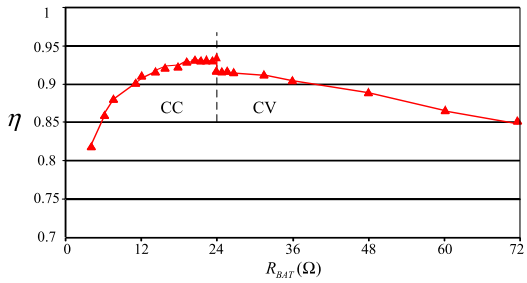

Fig. 18. Measured efficiency versus the equivalent battery load.

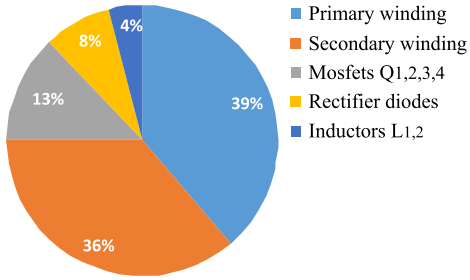

Fig. 19. Power loss breakdown among circuit components at R_{BAT} of 24 Ω in CC mode.

the measured resonant currents. Fig. 19 shows that the primary and secondary windings of loosely coupled transformer dissipate most of the power loss because of their relatively larger resonant currents than the other components at the CC mode charging condition.

V. Conclusion

In this paper, an *LCC–LCC* compensated IPT converter is designed to achieve the ZPA and load-independent CC and CV output for battery charging applications. This paper also proposed a design method to combat the constraints imposed by the IPT transformer and input dc voltage. The characteristic of load-independent output permits the implementation of a simple duty cycle control at two fixed frequencies. Moreover, the sensitivity of the converter output and input impedance against variation of compensation components is analyzed. It is found that near zero reactive power and soft switching of the power switches with high output current and voltage accuracy can be maintained over a wide operating range. The design method in this paper can be extended to the other higher order compensation topologies with more design freedom.

References

[1] Y. Jang and M. M. Jovanović, "A contactless electrical energy transmission system for portable-telephone battery chargers," *IEEE Trans. Ind. Electron.*, vol. 50, no. 3, pp. 520–527, Jun. 2003.

[2] B. Choi, J. Nho, H. Cha, T. Ahn, and S. Choi, "Design and implementation of low-profile contactless battery charger using planar printed circuit board windings as energy transfer device," *IEEE Trans. Ind. Electron.*, vol. 59, no. 1, pp. 140–147, Feb. 2004.

[3] S. Y. Hui, "Planar wireless charging technology for portable electronic products and Qi," *Proc. IEEE*, vol. 101, no. 6, pp. 1290–1301, Jun. 2013.

[4] J. Sallán, J. L. Villa, and J. F. Sanz, "Optimal design of ICPT system applied to electric vehicle battery charge," *IEEE Trans. Ind. Electron.*, vol. 56, no. 6, pp. 2140–2149, Jun. 2009.

[5] G. A. Covic and J. T. Boys, "Inductive power transfer," *Proc. IEEE*, vol. 101, no. 6, pp. 1276–1289, Jun. 2013.
[6] S. Li and C. C. Mi, "Wireless power transfer for electric vehicle applications," *IEEE J. Emerg. Sel. Topics Power Electron.*, vol. 3, no. 1, pp. 4–17, Mar. 2015.
[7] Z. Li, C. Zhu, J. Jiang, K. Song, and G. Wei, "A 3-kW wireless power transfer system for sightseeing car supercapacitor charge," *IEEE Trans. Power Electron.*, vol. 32, no. 5, pp. 3301–3316, May 2017.
[8] X, Liu and S. Y. R. Hui, "Equivalent circuit modeling of a multilayer planar winding array structure for use in universal contactless battery charging platform," *IEEE Trans. Power Electron.*, vol. 22, no. 1, pp. 21–29, Jan. 2007.
[9] J, Achterberg, E. A. Lomonova, and J. de Boeij, "Coil array structures compared for contactless battery charging platform," *IEEE Trans. Magn.*, vol. 44, no. 5, pp. 617–622, May 2008.
[10] Popular Sci., "Tesla car can be summoned and park itself," 2016. [Online] Available: https://www.popsci.com/creeping-toward-kitt-now-tesla-can-be-summoned-and-park-itself-video
[11] Nissan Motor Corporation, Yokohama, Japan, "Wireless charging system," 2017. [Online] Available: https://www.nissan-global.com/EN/TECHNOLOGY/OVERVIEW/wcs.html
[12] W. Zhang, S. C. Wong, C. K. Tse, and Q. Chen, "Load-independent duality of current and voltage outputs of a series or parallel compensated inductive power transfer converter with optimized efficiency," *IEEE J. Emerg. Sel. Topics Power Electron.*, vol. 3, no. 1, pp. 137–146, Mar. 2015.
[13] W. Zhang and C. C. Mi, "Compensation topologies of high-power wireless power transfer systems," *IEEE Trans. Veh. Technol.*, vol. 65, no. 6, pp. 4768–4778, Jun. 2016.
[14] X. Qu, Y. Jing, H. Han, S. C. Wong, and C. K. Tse, "Higher order compensation for inductive-power-transfer converters with constant voltage or constant-current output combating transformer parameter constraints," *IEEE Trans. Power Electron.*, vol. 32, no. 1, pp. 394–405, Jan. 2017.
[15] S. Li, W. Li, J. Deng, T. D. Nguyen, and C. Mi, "A double-sided LCC compensation network and its tuning method for wireless power transfer," *IEEE Trans. Veh. Technol.*, vol. 64, no. 6, pp. 2261–2273, Jun. 2015.
[16] H. Feng *et al.*, "An LCC-compensated resonant converter optimized for robust reaction to large coupling variation in dynamic wireless power transfer," *IEEE Trans. Ind. Electron.*, vol. 63, no. 10, pp. 6591–6601, Oct. 2016.
[17] T. Kan, T. D. Nguyen, J. C. White, R. K. Malhan, and C. Mi, "A new integration method for an electric vehicle wireless charging system using LCC compensation topology: Analysis and design," *IEEE Trans. Power Electron.*, vol. 32, no. 2, pp. 1638–1650, Feb. 2017.
[18] Z. Huang, S. C. Wong, and C. K. Tse, "Design of a single-stage inductive-power-transfer converter for efficient EV battery charging," *IEEE Trans. Veh. Technol.*, vol. 66, no. 7, pp. 5808–5821, Jul. 2017.
[19] J. Lu, G. Zhu, D. Lin, S. C. Wong, and J. Jiang, "Load-independent voltage and current transfer characteristics of high-order resonant network in IPT system," *IEEE J. Emerg. Sel. Topics Power Electron.*, to be published.
[20] X. Qu, H. Han, S. C. Wong, and C. K. Tse, "Hybrid IPT topologies with constant-current or constant-voltage output for battery charging applications," *IEEE Trans. Power Electron.*, vol. 30, no. 11, pp. 6129–6337, Nov. 2015.
[21] R. Mai, Y. Chen, Y. Li, Y. Zhang, G. Cao, and Z. He, "Inductive power transfer for massive electric bicycles charging based on hybrid topology switching with a single inverter," *IEEE Trans. Power Electron.*, vol. 32, no. 8, pp. 5897–5906, Aug. 2017.
[22] V. B. Vu, D. H. Tran, and W. J. Choi, "Implementation of the constant current and constant voltage charge of inductive power transfer systems with the double-sided LCC compensation topology for electric vehicle battery charge applications," *IEEE Trans. Power Electron.*, vol. 33, no. 9, pp. 7398–7410, Sep. 2018.
[23] *Wireless Charging of Electric and Plug-in Hybrid Vehicles*, SAE Int. Standard J2954, 2010. [Online] Available: http://standards.sae.org/wip/j2954/
[24] U. K. Madawala and D. J. Thrimawithana, "A bidirectional inductive power interface for electric vehicles in V2G systems," *IEEE Trans. Ind. Electron.*, vol. 58, no. 10, pp. 4789–4796, Oct. 2011.
[25] X. Qu *et al.*, "Wide design range of constant output current using double-sided LC compensation circuits for inductive power transfer applications," *IEEE Trans. Power Electron.*, to be published.
[26] O. Knecht and J. W. Kolar, "Performance of series-compensated IPT systems for high power transcutaneous energy transfer," *IEEE Trans. Power Electron.*, to be published.

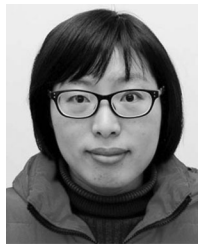

Xiaohui Qu (S'08–M'10) received the B.Eng. and M.Eng. degrees in electrical engineering from the Nanjing University of Aeronautics and Astronautics, Nanjing, China, in 2003 and 2006, respectively, and the Ph.D. degree in power electronics from The Hong Kong Polytechnic University, Hong Kong, in 2010.

In 2010, she joined the School of Electrical Engineering, Southeast University, Nanjing, China, where she is currently a Full Professor with research focus on power electronics. From January 2015 to January 2016, she was a Visiting Scholar with the Center of Reliable Power Electronics, Aalborg University, Denmark. Her current research interests include LED lighting systems, wireless power transfer, and power electronics reliability.

Dr. Qu was a recipient of the Outstanding Reviewer Award and the Prize Paper Award from IEEE Transactions on Power Electronics in 2017 and 2018.

Haijun Chu received the B.Eng. degree in electrical engineering from the Nanjing Institute of Technology, Nanjing, China, in 2016. He is currently working toward the M.Eng. degree in electrical engineering at Southeast University, Nanjing, China.

His current research interest mainly includes wireless power transfer.

Siu-Chung Wong (M'01–SM'09) received the B.Sc. degree in physics from the University of Hong Kong, Hong Kong, in 1986, the M.Phil. degree in electronics from The Chinese University of Hong Kong, Hong Kong, in 1989, and the Ph.D. degree from the University of Southampton, Southampton, U.K., in 1997.

He is currently an Associate Professor with the Department of Electronic and Information Engineering, The Hong Kong Polytechnic University, Hong Kong, where he conducts research in power electronics.

Dr. Wong is an Associate Editor for the IEEE TRANSACTIONS ON CIRCUITS AND SYSTEMS II, an Editor for the *Energy and Power Engineering Journal*, and a Member of the editorial board of the *Journal of Electrical and Control Engineering*.

Chi K. Tse (M'90–SM'97–F'06) received the B.Eng. (Hons.) degree in electrical engineering and the Ph.D. degree from the University of Melbourne, Melbourne, VIC, Australia, in 1987 and 1991, respectively.

He is currently the Chair Professor with Hong Kong Polytechnic University, Hong Kong, where he served as the Head of the Department of Electronic and Information Engineering, from 2005 to 2012. His research interests include power electronics, nonlinear systems, and complex network applications.

Prof. Tse was a recipient of a number of research and industry awards, including Prize Paper Awards by IEEE TRANSACTIONS ON POWER ELECTRONICS in 2001, 2015, and 2018, RISP Journal of Signal Processing Best Paper Award in 2014, Best paper Award by International Journal of Circuit Theory and Applications in 2003, two Gold Medals at the International Inventions Exhibition in Geneva in 2009 and 2013, and a Silver Medal at the International Invention Innovation Competition in Canada in 2016. He is currently serving as an Editor-in-Chief for the IEEE TRANSACTIONS ON CIRCUITS AND SYSTEMS II (2016–2019). He has also served as an Editor-in-Chief for IEEE CIRCUITS AND SYSTEMS MAGAZINE (2012–2015), IEEE CIRCUITS AND SYSTEMS SOCIETY NEWSLETTER (since 2007), and is on the editorial boards of a few other journals.